POLYOXOMETALATES

Open Access
REVIEW ARTICLE

Polyoxometalate-based one-dimensional subnanomaterials

Yifan Qin, Rongzhu Ma, and Simin Zhang

MOE Key Laboratory of Cluster Science, School of Chemistry and Chemical Engineering, Beijing Institute of Technology, Beijing 100081, China

Cite This: *Polyoxometalates*, **2026**, *5*, 9140117

Read Online

ABSTRACT: One-dimensional (1D) subnanomaterials (SNMs), including subnanowires (SNWs) and subnanobelts (SNBs), have diameters or thicknesses comparable to the unit cell size and exhibit polymer-like properties, such as rheology, gelling, and adhesion, owing to their dimensional similarity to polymer chains. Originally, single-component 1D SNMs were dominant, but the development of the cluster-nuclei coassembly (CNCA) strategy has enabled the fabrication of various polyoxometalate (POM)-based 1D SNMs with precisely controlled compositions and structures. In this review, a variety of SNWs and SNBs, including POM, metal cluster-POM, metal cation-POM, metal oxide-POM, metal sulfide-POM, and high-entropy oxide-POM materials, are discussed, paying particular attention to their synthesis, programmable structures, polymer - like properties, and excellent performance in gelling, adhesion, catalysis, polarization, and photothermal conversion applications. Moreover, the outstanding processability of 1D SNMs, which enables the construction of macroscale assemblies with expanded applicability, such as fibers, films, and gels, is described. Finally, challenges and future directions are discussed, providing new viewpoints on the development and applications of POM-based 1D SNMs.

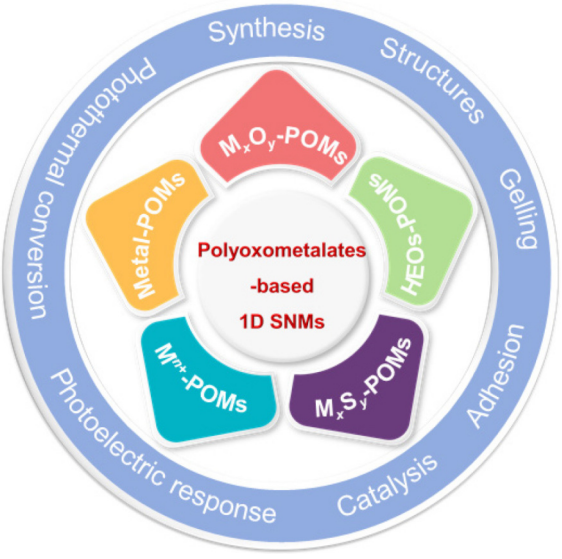

KEYWORDS: polyoxometalates, subnanowires, subnanobelts, cluster-nuclei co–assembly strategy, applications

1 Introduction

The subnanometer scale is considered a critical transitional region between molecular systems and nanomaterials [1]. Subnanomaterials (SNMs) are nanomaterials having the size of a single unit cell (e.g., 0.5–1.9 nm) in at least one dimension [2]. When the size decreases to the subnanometer scale, changes in electronic structure and topological morphology lead to a qualitative leap in the material properties [2–4]. Compared with conventional nanoscale materials, SNMs exhibit an ultrahigh aspect ratio [5], more active sites, and distinctive properties such as self-assembly behavior and polymer-like properties [6–10].

Among the SNMs, one-dimensional (1D) SNMs, including subnanowires (SNWs) and subnanobelts (SNBs), are characterized by a diameter or thickness close to the size of a single unit cell [11]. Owing to their similar size and topology structures to polymer chains, 1D SNMs exhibit polymer-like properties, including conformation, rheology, gelling, and adhesion [12, 13]. The synthesis of 1D SNMs usually requires anisotropic growth in a certain dimension. Originally, single-component 1D SNMs, such as GdOOH SNWs [4], SnO_2 SNWs [14], tungsten oxide SNBs [9], indium sulfide SNBs [15], and tungsten bronze SNWs [16], were mainly synthesized via the directed growth of nuclei under good–poor solvent conditions. Mechanistically [17], the good–poor solvent system confines the nuclei to a single unit-cell size by regulating supersaturation. Then, nuclei at single-unit cells undergo controlled epitaxial growth into diverse 1D SNMs, with their ultimate morphology and growth direction being determined by ligand detachment from the initial nuclei and the oriented attachment of building blocks. The strong ligand–nuclei interactions impose a dimensional constraint: 1D epitaxial growth proceeds with less ligand detachment on one crystal face; in contrast, two-dimensional or three-dimensional (3D) growths are kinetically hindered by ligand detachment on different faces. In addition, according to the theory of the transition state [17], the high state similarity between the building blocks and existing structures leads to a minimal energy difference for 1D growth, resulting in a lower energy barrier relative to other dimensional growth pathways and facilitating the formation of 1D nanostructures. This thermodynamic control during nucleation is crucial for the bottom-up construction of well-defined

Received: November 27, 2025; **Revised:** January 7, 2026
Accepted: January 18, 2026

Address correspondence to zhangsimin@bit.edu.cn

https://doi.org/10.26599/POM.2026.9140117

subnanometer structures. Later, Wang's group developed the cluster-nuclei coassembly (CNCA) strategy to fabricate 1D SNMs [18]. Specifically, at the nucleation stage of inorganic nuclei, polyoxometalate (POM) clusters are introduced to intervene in the growth of nuclei into the subnanometer scale. The subnanometric sizes of POMs match the sizes of inorganic nuclei; meanwhile, the strong dipole–dipole attraction between clusters and nuclei favors their tight contact. Driven by the dipole–dipole energy, which canbe expressed as $W_{\mu-\mu}(r,\theta',\phi)=\frac{\mu_i\mu_j\cos\theta'_j}{4\pi\varepsilon_0\varepsilon r_{ij}{}^3}(\cos\theta'_i)(\cos\theta'_j)[2+2kr_{ij}+(kr_{ij})^2]$ [14, 19], the POM–nuclei building blocks are oriented and aggregated along the dipole axis and finally coassemble into diverse multicomponent block polymer-like 1D SNMs, such as MoO_3-POM SNBs [20], Au-PW_{12} SNWs [21], Ag-POM SNWs [22] and Bi_2O_3-PMA SNWs [23]. Another route to 1D SNMs relies on the anisotropic assembly of single POM clusters, triggered by the formation of anisotropic surfaces on them. In this case, noncovalent interactions drive the anisotropic assembly of POM clusters into diverse single-cluster 1D SNMs.

POMs are a distinctive class of subnanometric clusters characterized by electron-rich structures, oxygen-enriched surfaces, and abundant substitutional sites [24–26]. Their chemical composition and structure can be precisely engineered at the molecular level, offering a robust foundation for oriented assembly [27]. To date, POMs have served as essential building blocks for constructing 1D SNMs [18, 28, 29]. Their similar size and topology to polymer chains endow POM-based 1D SNMs with polymer-like properties, such as conformation, rheology, gelling, and adhesion [13]. As a result, POM-based 1D SNMs can be processed into fibers or films using polymer techniques including electrospinning [30] and wet spinning [23], thereby expanding the morphological variety of their macroscopic assembly. In addition, POMs not only contribute to size constraints but also facilitate extensive electron delocalization across 1D SNMs [31]. The electron delocalization, arising from atomic orbital overlap, provides abundant active sites and enhances interaction with external fields, making POM-based 1D SNMs highly suitable for catalytic applications [31, 32]. The synergistic effect of POM functionality and subnanoscale structural features further endows these 1D POM-based assemblies with superior charge transfer behavior and promising performance in energy conversion and photothermal systems [33–35].

This review summarizes representative examples of POM-based 1D SNMs, focusing on synthetic methods, their unique properties, and applications in gelling, adhesion, catalysis, and photothermal/electrochemical energy conversion. This work provides a comprehensive perspective on the synthesis, structures, assemblies, and applications of POM-based 1D SNMs.

2 POM-based 1D SNMs

Facilitated by their subnanometer sizes and strong interactions, POM clusters and inorganic nuclei can form tightly bonded units, which then act as complementary building blocks for subsequent coassembly into various 1D SNMs. Using the CNCA strategy and various POMs as the building blocks, e.g., $[Mo_6O_{19}]^{2-}$, $[Mo_8O_{26}]^{4-}$, $[PMo_{12}O_{40}]^{3-}$ (PMA), and $[PW_{12}O_{40}]^{3-}$ (PTA), 1D SNMs including POM single-cluster, metal cluster-POM (M-POM), metal cation-POM (M^{n+}-POM), metal oxide-POM (M_xO_y-POM), metal sulfide-POM (M_xS_y-POM), and high-entropy oxide-POM (HEO-POM) 1D SNMs have been developed.

2.1 POM single-cluster 1D SNMs

POMs have oxygen-rich surfaces and numerous substitutional sites [25, 26]. Unlike conventional nanoparticles, the rich substitution chemistry of POMs enables the gradual regulation of building blocks by tailoring charge and surface features, leading to targeted ligand attachment and surface energy regulation.

The unsaturated coordination of surface atoms in SNMs results in extremely high surface energy and entropy, inducing substantial surface atomic rearrangements and structural distortions [1]. Generally, the molecular-level programmable interactions of POMs that drive the self-assembly allow 1D SNMs to self-distort at specific angles to minimize surface energy, enabling the formation of helical nanostructures with tunable helicity. Consequently, diverse chiral conformations can be generated without any chiral molecular assistance. For instance, Liu's [35] reported that the self-assembly of POM clusters into helical SNBs was driven by controlled surface energy, achieved by the competing binding of Ca^{2+} and quaternary ammonium cation (CTA^+) ligands (Fig. 1(a)). When lower Ca^{2+} concentrations were used in the synthesis, both left-handed and right-handed SNBs were formed. In contrast, high Ca^{2+} concentrations led to the release of CTA^+ ligands, increasing surface energy and driving the evolution of SNBs from helices to nanorings or nanotubes with higher curvature (Figs. 1(b)–1(d)). Homochiral isomers could be immobilized by introducing additional chiral molecules. From a thermodynamic perspective, a positive entropy change was required to offset the rise in surface energy (based on $\Delta G = \Delta H - T\Delta S$) [35], which can be produced by morphological transitions from SNBs to helical structures and helical nanobelts to nanorings and nanotubes. This entropy gain likely originates from the increased conformational degrees of freedom and higher structural disorder in the curved and coiled architectures compared with their planar or linear precursors, providing the thermodynamic driving force for these transformations. Furthermore, chiral molecules directed the selective assembly of chiral POM-based SNBs, which exhibited strong circular dichroism signals in both solution and solid-film states. By modulating the ratio of POM, CTA^+, and Ca^{2+}, the helicity of the resulting assemblies can be finely controlled, enabling precise morphological tuning and the corresponding modulation of their chiroptical responses. In addition, as a result of a pronounced chiral-induced spin selectivity effect, these chiral POM-based assemblies can function as effective chiral light detectors, exhibiting distinct photoresponses to left- and right-circularly polarized light (Fig. 1(e)).

The assembly of POM clusters into subnanometric structures remains crucial yet challenging, primarily owing to the lack of connecting mediators [36]. This process requires appropriate driving forces to promote cluster aggregation and necessitates precise size control to suppress spontaneous crystallization and overgrowth. In the case of highly symmetric POMs, their isotropic surface properties hinder the directional assembly required for the growth of 1D SNMs due to the absence of anisotropic sites. As a result of efforts to solve this issue, POM clusters with unique electronic structures and asymmetric atomic distributions have been fabricated [37]. For instance, two giant five-shell POM molecular cages (MCs) were synthesized via a typical combination procedure using $\{PW_{12}\}$ and metal ions. The resulting POM-based MCs exhibited a size of ~ 3.5 nm and comprised three structurally distinct components: M6-substituted trilacunary Keggin-type $\{PW_9\}$ clusters, Mn-bridged $\{W_4\}$ units, and templating metal

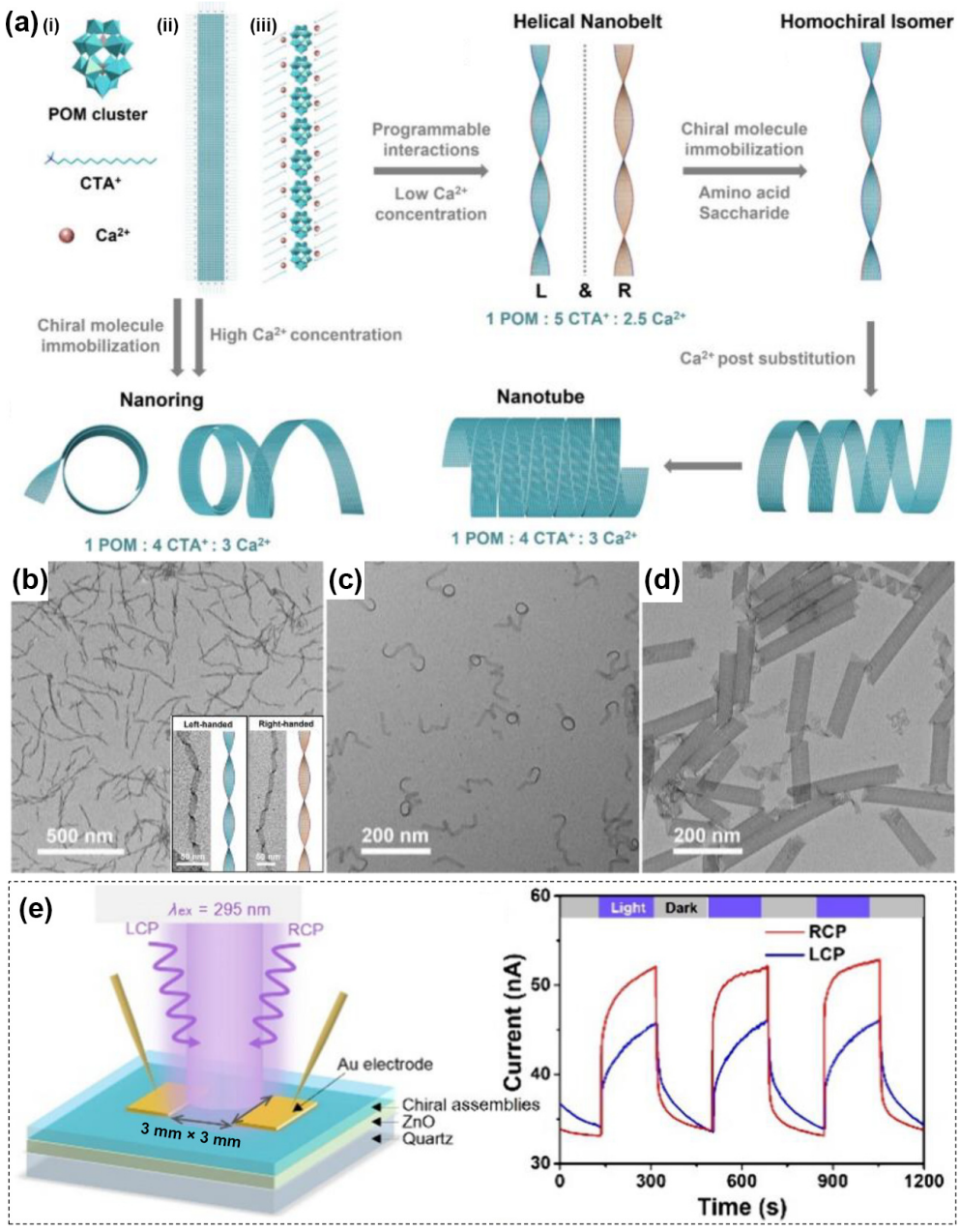

Figure 1 POMs single-cluster nanobelts. (a) Programmable synthesis of POM helical assemblies. TEM images of (b) POM helical nanobelts (inset: L- (left) and R- (right) enantiomers). (c) POM nanorings and (d) POM nanotubes. (e) Circularly polarized light (CPL) photodetection. Reproduced or adapted with permission from Ref. [35], © American Chemical Society 2024.

cation clusters that directed the overall assembly (Fig. 2(a)). Such POM-based MCs exhibited good stability in aqueous solutions, maintaining monodispersity. This allowed fabricating single-cluster nanowires using the POM-based MCs and CTA^+ as a surfactant (Fig. 2(a)). The resulting nanowires possessed diameters of 3.96 nm, far beyond the defined size, attributed to the large size of the single POM-based MC and the entangled ligands on the surface. The electronic interaction between the POM-based MCs and CTA^+ ligands enabled controlled growth, ultimately yielding single-cluster nanowires in the chloroform phase. During assembly, amphiphilic CTA^+ ligands promoted a transition from an isotropic electrostatic potential energy to directional assembly guided by hydrophobic interactions between alkyl chains, enabling the precise, tunable construction of 1D nanowires from 0D clusters and thereby realizing the directional assembly of POMs.

Nevertheless, in most cases, symmetry interactions between POMs result in diverse nondirectional shapes [38]. By introducing lacuna or substitutional metal atoms into the POM cluster structure, anisotropic connective sites can be created, enabling oriented self-assembly [39–41]. Using this strategy, a series of single-cluster SNWs was developed, employing mono-metal-substituted Dawson-type clusters $[MP_2W_{17}O_{61}]^{n-}$ as building blocks [28]. As shown in Fig. 2(b), SNWs with a uniform single-cluster size in diameter were synthesized under neutral conditions (pH 6.5). The single-cluster SNWs exhibited an ultrahigh aspect ratio, resulting in superior flexibility and assembly tendency to form bundle structures. In the connected structure, acetate molecules serve as linkers to tether two POM clusters in a head-to-head configuration,

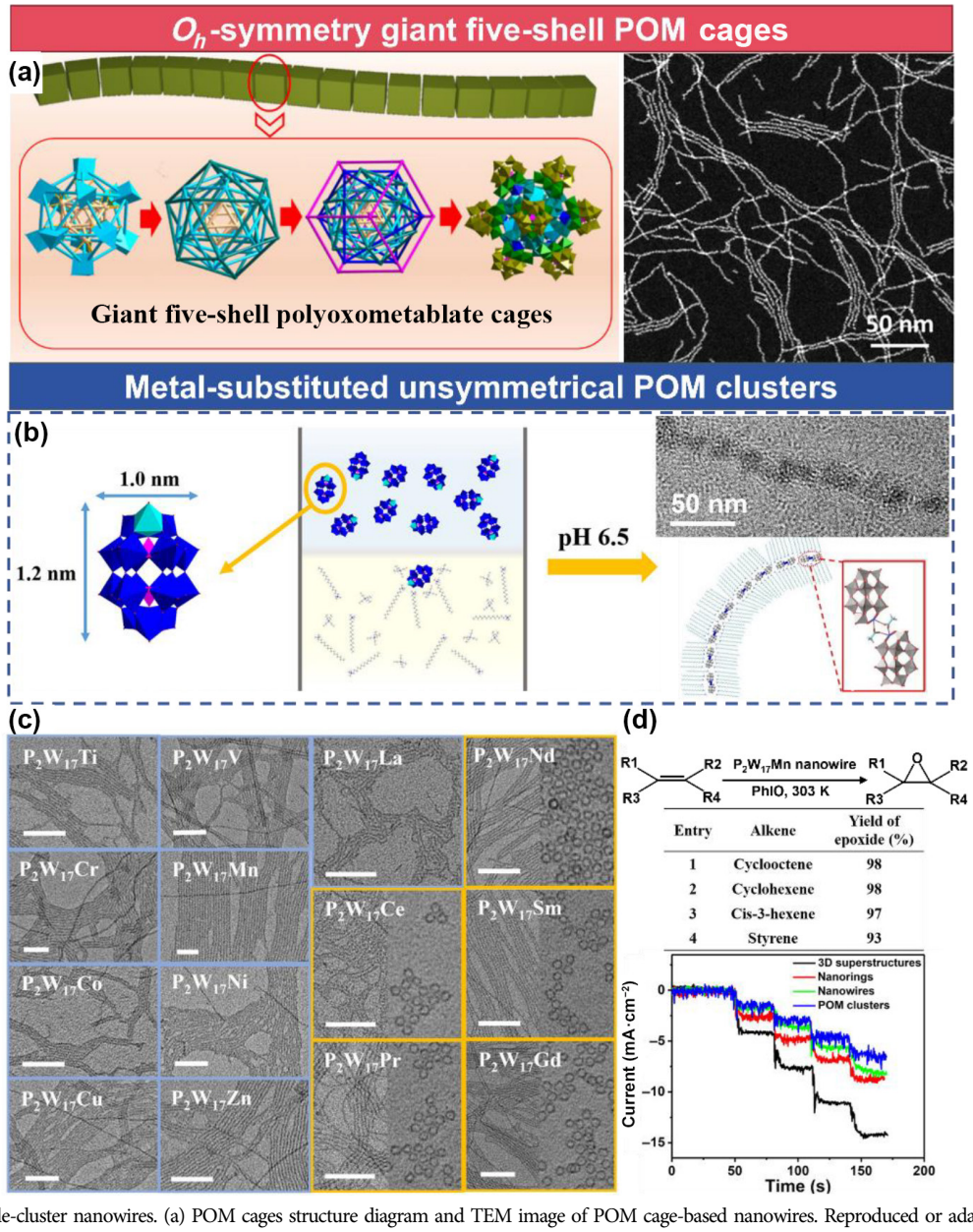

Figure 2 POMs single-cluster nanowires. (a) POM cages structure diagram and TEM image of POM cage-based nanowires. Reproduced or adapted with permission from Ref. [37], © American Chemical Society 2025. (b) Illustration of the synthetic procedure to metal-substituted POM cluster-based nanowires. (c) Gallery of nanowires constructed by $P_2W_{17}M$ clusters. (d) Catalytic and electrochemical sensing performances. Reproduced or adapted with permission from Ref. [28], © Liu, Q. D., et al., some rights reserved; exclusive licensee American Association for the Advancement of Science 2019. No claim to original U.S. Government Works. Distributed under a Creative Commons Attribution NonCommercial License 4.0 (CC BY-NC).

forming dimers. Then, weak interactions, including electrostatic and van der Waals forces, connect these dimers (Fig. 2(b)). The connection configuration and angle was controlled by adjusting the system pH. In addition, 15 types of metals were used to fabricate metal-substituted POMs as building blocks for the manufacture of single-cluster SNWs. In addition, some of these POMs self-assembled into superstructures (Fig. 2(c)). In particular, single-cluster $P_2W_{17}Mn$ SNWs exhibited excellent catalytic activity for olefin epoxidation, and its 3D superstructures displayed enhanced sensitivity to H_2O_2 detection (Fig. 2(d)).

2.2 M-POM 1D SNMs

.

The mechanism of the CNCA strategy is shown in Fig. 3(a). In the CNCA strategy, metal-atom clusters are added to participate in nucleation and the growth of nuclei [18], serving as building blocks for 1D SNMs. Subsequently, these building blocks can coassemble with POM clusters via electrostatic forces and coordination interactions, enabling a bottom-up approach that furnishes 1D SNMs with a precise architecture and tailored properties. Using this approach, A–B–A–B-type $AuPW_{12}$ building blocks in which Au_{18} clusters were attached to the surface of POMs via absorption on the bridge oxygen sites of PTA clusters were obtained (Fig. 3(b)) [21]. Then, the growth of this A–B–A–B-type coassembly afforded alternating polymer-like SNWs with a diameter of ~ 1 nm. In the alternating heterostructures, electrons are transferred from the PTA to the Au_{18} cluster surface, resulting in a negative shift in binding energy. Benefiting from the electron-rich surface, POMs can serve

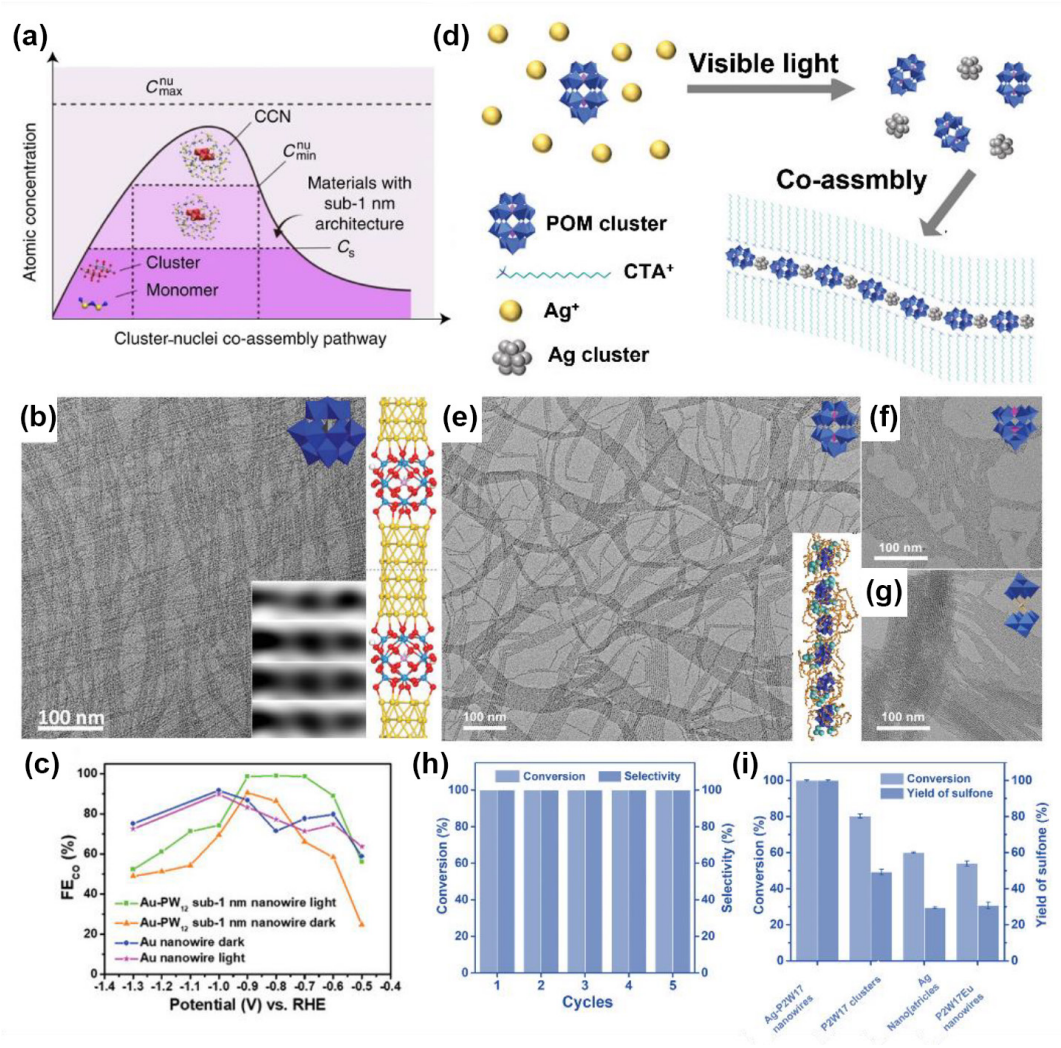

Figure 3 M-POM 1D SNMs with "A–B–A–B" type configuration controlled by CNCA strategy. (a) Diagram of the CNCA pathway for forming subnanostructures. Reproduced or adapted with permission from Ref. [18], © Liu, J. L. et al., under exclusive licence to Springer Nature Limited 2019. (b) TEM image and molecular model of Au-PW_{12} SNWs (inset: cryo-TEM image of Au-PW_{12} SNWs). (c) The catalytic performance for CO_2 reduction. Reproduced or adapted with permission from Ref. [21], © Wiley-VCH GmbH 2020. (d) Synthesis illustration of Ag-POM SNWs. TEM images of Ag-POM SNWs constructed by different POM clusters: (e) $[P_2W_{17}O_{62}]^{10-}$, (f) $[P_2W_{15}O_{56}]^{12-}$, (g) $[EuW_{10}O_{36}]^{9-}$. (h)–(i) Catalytic performance in thioether oxidations with H_2O_2. Reproduced or adapted with permission from Ref. [22], © Wiley-VCH GmbH 2022.

as electron donors and Au_{18} clusters as acceptors, promoting the formation of $COOH^*$ intermediates on the $AuPW_{12}$ catalyst surface, thereby achieving effective photoelectrocatalytic activity for the reduction of CO_2 to CO (Fig. 3(c)).

In addition to the highly topological, symmetric POM clusters, some low-symmetry POM clusters can also be used as building blocks to construct 1D SNMs. Thus, A–B–A–B-type Ag-POM periodic SNWs were synthesized [22] using $[P_2W_{17}O_{61}]^{10-}$, $[P_2W_{15}O_{56}]^{12-}$, and $[EuW_{10}O_{36}]^{9-}$ POM clusters with anisotropic surface properties (Figs. 3(e)–3(g)). In this system, Ag atoms are initially oxidized to Ag^+ ions on the POM surface and then aggregate into Ag clusters, which coassemble with POM clusters into alternately arranged oriented SNWs driven by visible light (Fig. 3(d)). The Ag–O direct bonding between Ag and POM clusters within this heterostructure facilitates highly efficient electron transfer, considerably enhancing the redox reaction performance (inset in Fig. 3(e)). The resulting Ag-POM SNWs exhibited ultrahigh specific area and single-cluster width, favoring size-dependent catalytic performance. Owing to the electron-rich nature of POM clusters and the subnanometric structures, Ag-POM SNWs are excellent candidates as catalysts for redox reactions (Fig. 3(h)). In the presence of 1 mM H_2O_2, the SNWs generated an extraordinary amperometric response, surpassing the signals from Ag nanoparticles and P_2W_{17} clusters by 2–4 orders of magnitude (Fig. 3(i)). Conclusively, the improvement in redox reactions can be attributed to the synergistic effect of the atom-level-precise structure and enhanced electron transfer within the coassembly heterostructure.

2.3 M^{n+}-POM 1D SNMs

Beyond periodic heterojunction SNWs, M^{n+}-POM SNWs are constructed from cation-bridged POM clusters. Benefiting from their oxygen-enriched and electron-rich surfaces, POM clusters can coordinate with metal cations. In a two-phase system, oriented SNWs composed of metal cations and POMs can be prepared via electrostatic and van der Waals interactions. Recently, alkaline earth cation-bridged PTA cluster SNWs with a width of ~ 1 nm were developed using a facile room-temperature stirring approach

(Fig. 4(a)) [42]. Specifically, Ca-PTA SNWs were constructed by bridging Ca^{2+} cations and PTA anion clusters with a linear alignment using a modified CNCA method (Figs. 4(a) and 4(b)). Oleylamine (OM) and protonated OM were intertwined around the SNWs via coordination interactions and electronic forces (Fig. 4(b)). Owing to their similar size to polymer chains, Ca-PTA SNWs exhibited high flexibility, transforming from coils into nanorings in ethanol (Fig. 4(a) inset). They can also spontaneously entangle to form 3D networks via physical crosslinking, trapping over 10 kinds of volatile organic liquids into freestanding organogels with a critical gelation concentration as low as 0.53%, driven by multiple interactions (Figs. 4(c) and 4(d)). This excellent organic liquid-collecting performance endows Ca-PTA SNWs with potential oil-spill recovery capacity (Fig. 4(e)).

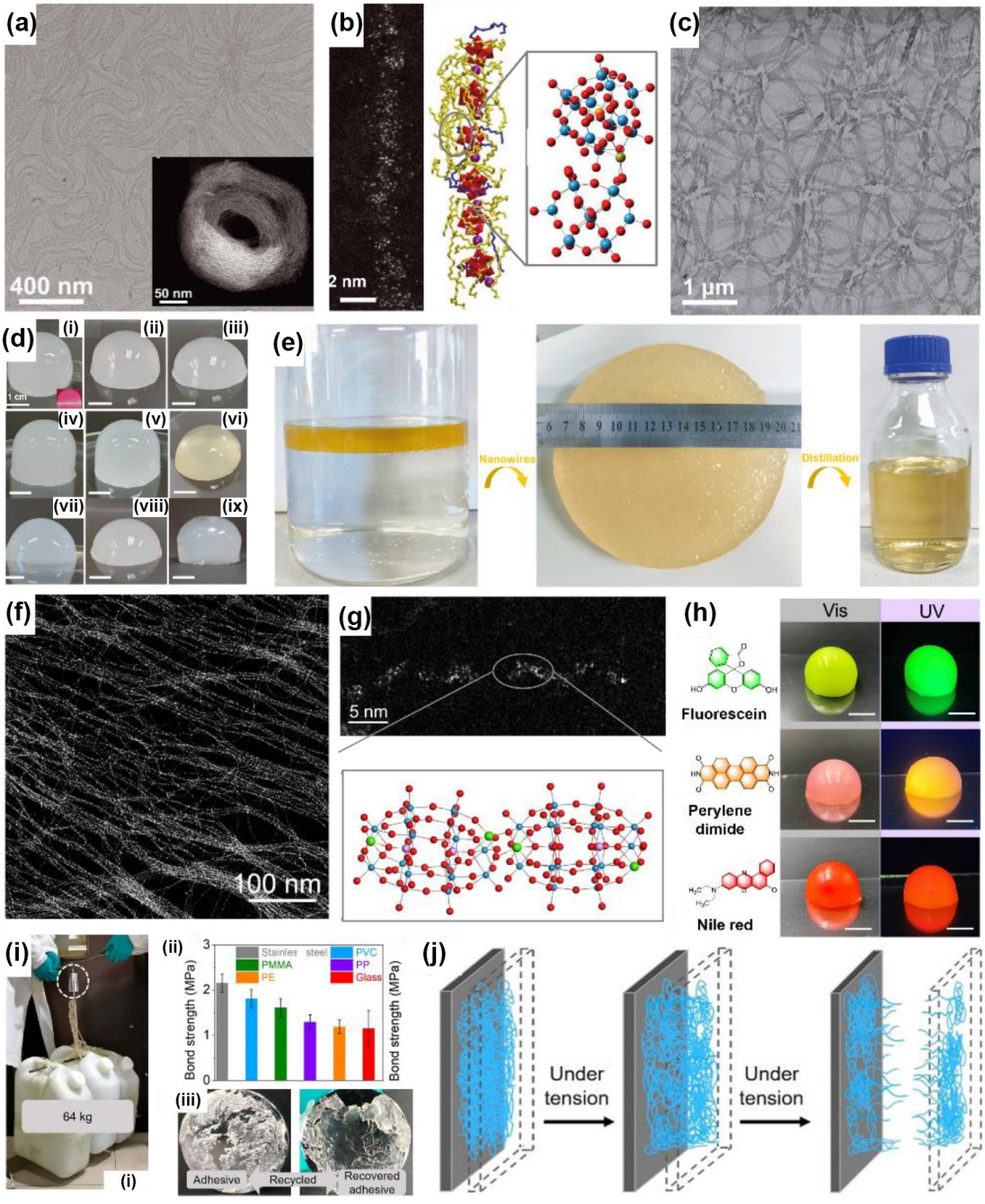

Figure 4 M^{n+}-POM 1D SNMs. (a) TEM image of Ca-PW_{12} SNWs. Inset: coiled SNWs. (b) HRTEM image and molecular model of a single SNW. (c) TEM image of nanowire networks of SNW-octane gel. (d) Photos of SNW-organic liquids gels: (i) octane, (ii) cyclohexane, (iii) hexane, (iv) toluene, (v) 2,5-dimethyl-2,5-di-(tert-butylperoxy) hexane, (vi) petrol, (vii) n-propyl ether, (viii) 1-dodecanethiol, and (ix) octadecene. (e) Oil spill recovery performance of Ca-PW_{12} SNWs. Reproduced or adapted with permission from Ref. [42], © Zhang, S. M., et al., some rights reserved; exclusive licensee American Association for the Advancement of Science 2022. No claim to original U.S. Government Works. (f) and (g) STEM images of Ca_2-P_2W_{16} NWs constructed by $K_6P_2W_{18}O_{62}$ clusters. Inset of (g): molecular model of Ca_2-P_2W_{16} NW structure. (h) Fluorescence of Ca_2-P_2W_{16} NW-based gels. Scale bar: 1 cm. Reproduced or adapted with permission from Ref [43], © Zhang, F. H., et al. 2023. (i) Adhesive performance of Ca-PW_{12} SNWs. (j) Adhesive mechanism of the Ca-PW_{12} SNWs adhesive. Reproduced or adapted with permission from Ref. [13], © American Chemical Society 2022.

Building upon these Ca-POM SNWs, more highly charged Dawson-type $[Ca_2P_2W_{16}O_{60}]^{14-}$ clusters were used as building blocks to construct SNWs with effectively controlled surface ligand density, enhancing the mechanical properties of organogels (Fig. 4(f)) [43]. The partial absence of metal-atom centers in the lacunary $[P_2W_{16}O_{60}]^{14-}$ clusters resulted in highly charged surfaces, which strongly promoted electrostatic interaction with Ca^{2+} and more surface-stabilizing cation ligands (e.g., protonated OM). Specifically, incorporating larger $[P_2W_{16}O_{60}]^{14-/13-}$ clusters interconnected by two Ca^{2+} ions at the junction points (Fig. 4(g)) increased the persistence length and substantially enhanced the rigidity of $Ca_2P_2W_{16}$ SNWs. As a result, $Ca_2P_2W_{16}$ SNW-based organogels outperformed Ca-PTA SNWs in terms of compressive strength and tensile strength. In addition, the organic phase in $Ca_2P_2W_{16}$ SNW-based organogels showed similar dynamic properties to liquid solvents. This allowed incorporating fluorescent dyes or groups into SNW-based organogels, endowing them with fluorescence properties and high-efficiency fluorescence energy conversion (Fig. 4(h)).

The entanglement network confers adhesive properties to M^{n+}-POM SNWs. Because of the strong cohesion among dried SNWs, Ca-PTA SNWs demonstrated versatile adhesive performance across various substrates, including glass, metals, and polymers, and can be easily recycled and removed (Fig. 4(i)) [13]. All SNW components, especially OM and protonated OM, interacted with substrates through electrostatic and van der Waals forces (Fig. 4(j)). The combination of strong cohesion and adhesion resulted in the excellent adhesive performance of Ca-PTA SNWs.

2.4 M_xO_y-POM 1D SNMs

Various well-defined POM clusters can be selected as the building blocks of M_xO_y-POM 1D SNMs, including Keggin-type clusters such as PMA, PTA, Lindqvist-type POMs like $[Mo_6O_{19}]^{2-}$ and $[W_6O_{19}]^{2-}$, as well as β-octamolybdate ($[Mo_8O_{26}]^{4-}$) and decatungstate ($[W_{10}O_{32}]^{4-}$).

Various high-quality M_xO_y-POM SNWs were synthesized using Fe_3O_4, Y_2O_3, Yb_2O_3, CeO_2, and Bi_2O_3 nuclei and PMA clusters (Fig. 5(a)) [23]. As demonstrated in the TEM images shown in Figs. 5(b) and 5(c), these SNWs possessed ultrahigh surface aspect ratios, with diameters of about 1 nm and lengths of several micrometers. The SNW components can be precisely regulated by tuning the M_xO_y nuclei, enabling the rational design of SNWs with tailored properties to meet specific functional requirements. For Fe_3O_4-PMA SNWs, the observed change in the valence states of Fe and Mo indicated the occurrence of electron transfer from Fe^{3+} ions to PMA clusters, demonstrating charge redistribution within the entire structure [44]. This directional electron flow stabilized the interfacial structure and enhanced overall redox efficiency, benefiting the catalytic performance.

Owing to their polymer-like properties, Bi_2O_3-PMA SNWs can be processed into freestanding films with excellent flexibility and toughness via the wet-spinning method (Fig. 5(f)). The resulting Bi_2O_3-PMA SNW films demonstrated not only good photothermal conversion performance [23], positioning them as promising materials for sustainable solar-driven water purification applications, but also strong absorbance and catalytic performance for lithium polysulfides (LPSs), making them potential separators for lithium–sulfur batteries (LSBs) [45]. The electron-localized nature of SNMs enhances light–matter interactions, enabling efficient photothermal energy conversion and, in turn, applications in seawater desalination. The Bi_2O_3-PMA SNW films exhibited a high absorption ratio of > 80% over a wide wavelength range of 250–2500 nm. They displayed a fast temperature increase from 25 to 64 °C within 5 min under 1 sun irradiation, whereas the temperature increase of Bi_2O_3-PMA nanorods was only 14.6 °C within 6 min (Fig. 5(g)). Furthermore, when applied to solar desalination, the Bi_2O_3-PMA SNW films effectively reduced the concentrations of key ions (Na^+, Mg^{2+}, K^+, and Ca^{2+}) in seawater by four orders of magnitude, meeting drinking standards (Fig. 5(h)). The superior photothermal performance of Bi_2O_3-PMA SNWs arises from their broad light absorption, enhanced by their subnanometric structure and intense localized surface plasmon resonance between metal ions (e.g., Mo^{5+} and Mo^{6+}) in PMA. When applied in LSBs [45], superaligned Bi_2O_3-PMA SNW films serve as interlayers to efficiently suppress LPS shuttling, greatly promoting the kinetics of LPS conversion and protecting Li anodes. Compared with a polypropylene (PP) film, the LSB with a superaligned Bi_2O_3-PMA SNW film as a separator delivered an enhanced capacity retention of 782 $mAh{\cdot}g^{-1}$ after 850 cycles (Fig. 5(i)). Under similar synthetic conditions, PMZ and PMT SNBs were successfully fabricated via the coassembly of PMA clusters with ZrO_2 and TiO_2 nuclei, respectively (Figs. 5(d) and 5(e)) [46]. The resulting products demonstrated superior catalytic activity and stability in oxidative desulfurization, outperforming the individual components (Figs. 5(j) and 5(k)). This successful extension of the synthesis strategy to PMZ and PMT systems confirms the universality of the CNCA approach and suggests that the strong interaction between PMA clusters and metal oxide nuclei creates unique active sites that contribute to outstanding catalysis and durability.

Using the CNCA strategy, four kinds of tungsten-based POMs were also introduced into a MoO_3 matrix, producing four distinct MoO_3-POM SNBs with a thickness of 1 nm [20]. Such SNBs possessed high flexibility, spontaneously coiling into spring-like structures (Figs. 5(n)(i) and 5(n)(ii)). Owing to the synergetic effect of the components and subnanostructures, the obtained MoO_3-POM SNBs exhibited efficient photothermal conversion performance and catalytic properties in the oxidation of thioethers at room temperature (Figs. 5(n)(iii) and 5(n)(iv)). The CNCA strategy also enabled the synthesis of 15 rare earth-based Mo-O SNWs, among which Ce-Mo-O SNWs demonstrated superior photocatalytic performance [47].

2.5 M_xS_y-POM 1D SNMs

By virtue of the universality of the CNCA strategy, the inorganic nuclei can also be extended to metal sulfide systems to construct M_xS_y-POM SNWs. As shown in Fig. 6, M_xS_y-POM SNWs composed of Cu_9S_5 nuclei and PTA clusters were prepared via CNCA [48]. During the nucleation of Cu_9S_5, PTA clusters were introduced and interacted with the nuclei through Cu–O coordination bonding, which confined their growth to a subnanometric scale (Fig. 6(a)). The resulting Cu_9S_5-PW_{12} SNWs exhibited an average width of 0.9 nm and good flexibility stemming from the inherent ultrathin structure (Figs. 6(b)–6(d)). The SNWs also exhibited remarkable electroreduction performance for CO_2. Unlike Cu_9S_5 nanowires, each unit of Cu_9S_5-PW_{12} SNWs can act as an independent catalytic site with distinct catalytic properties (Figs. 6(e)–6(g)). At a potential of −0.8 V (vs. RHE), the Cu_9S_5 SNWs achieved a Faraday efficiency (FE) for $HCOO^-$ generation as high as 82.0%, whereas that of Cu_9S_5 nanowires was only 29.6% (Fig. 6(e)). This enhancement was marked by a current density of

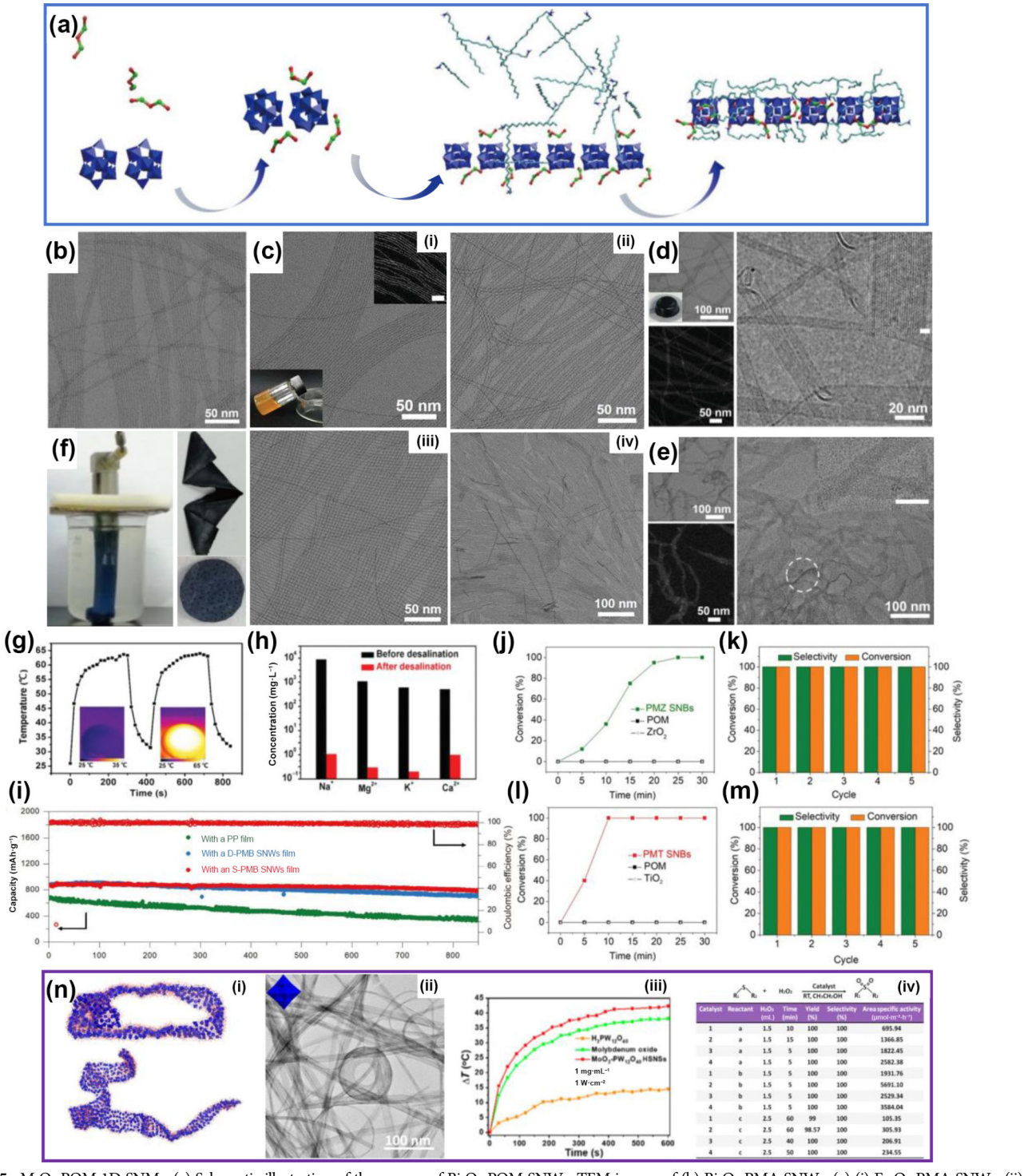

Figure 5 M_xO_y-POM 1D SNMs. (a) Schematic illustration of the process of Bi_2O_3-POM SNWs. TEM images of (b) Bi_2O_3-PMA SNWs, (c) (i) Fe_4O_3-PMA SNWs, (ii) Y_2O_3-PMA SNWs, (iii) Yb_2O_3-PMA SNWs, and (iv) Ce_2O_3-PMA SNWs, (d) PMZ SNBs, and (e) PMT SNBs. (f) Wet spinning films of Bi_2O_3-PMA SNWs. (g) and (h) Photothermal conversion and (i) LSB performance of Bi_2O_3-PMA SNW films. Reproduced or adapted with permission from Ref. [23], © Wiley-VCH GmbH 2021; Ref. [45], © Science China Press and Springer-Verlag GmbH Germany, part of Springer Nature 2021. (j)–(m) Catalytic performance for the oxidative desulfurization reaction of PMZ and PMT SNBs. (n) (i) Structure and (ii) TEM image of MoO_3-POMs SNBs, (iii) photothermal conversion, and (iv) catalytic performance. Reproduced or adapted with permission from Ref. [20], © American Chemical Society 2020.

3.20 mA·cm^{-2} at −0.9 V for the SNWs, highlighting the critical role of subnanometric structures in enhancing electrocatalytic performance (Fig. 6(f)). Meanwhile, the FE for CH_3CH_2OH generation by Cu_9S_5 nanowires was 21.5%, whereas Cu_9S_5-PW_{12} SNWs exhibited negligible efficiency (Fig. 6(g)). The results suggested that the confined catalytic area of single-cluster-size Cu_9S_5-PW_{12} SNWs selectively facilitated the synthesis of small molecules, as the limited space inherently restricts extensive molecular growth. In contrast, continuous, active crystal surfaces enabled C–C bond coupling to form diverse products. The synthesis and performance

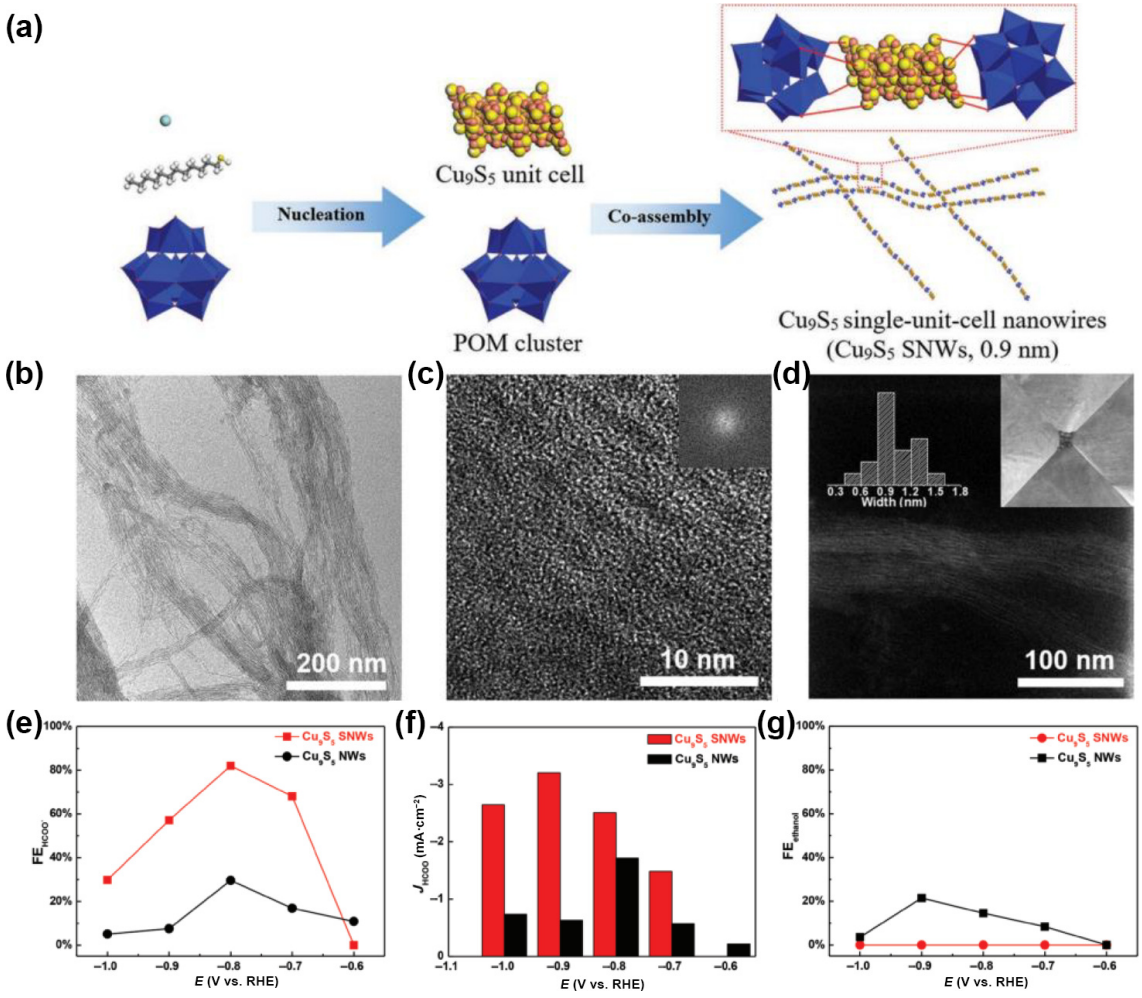

Figure 6 M_xS_y-POM SNWs. (a) Schematic illustration of process of Cu_9S_5-PW_{12} SNWs. (b) TEM, (c) HRTEM and (d) scanning transmission electron microscopy (STEM) images of Cu_9S_5-PW_{12} SNWs. (e) and (f) Electroreduction performance for CO_2. Reproduced or adapted with permission from Ref. [48], © Wiley-VCH GmbH 2021.

of Cu_9S_5-PW_{12} SNWs render them suitable for small-molecule precision catalysis.

2.6 HEO-POM 1D SNMs

HEO crystals are typically synthesized via high-temperature carbonization, which limits control over their structure and properties. The design of HEOs is based on Gibbs free energy (ΔG_{mix}), which can be expressed as $\Delta G_{mix} = \Delta H_{mix} - T\Delta S_{conf}$, where ΔH_{mix} and ΔS_{conf} represent the changes in mixing enthalpy and configurational entropy, respectively [49]. Compared with conventional HEO crystals, the unsaturated coordination of surface atoms in 1D SNMs leads to very high surface energy and entropy, causing surface atomic rearrangements and structural distortions [1]. According to this principle, additional surface entropy (ΔS_{sur}), which includes vibrational entropy (S_{vib}), translational entropy (S_{tra}), and rotational entropy (S_{rot}), can enhance the contribution of the total entropy change, enabling the low-temperature synthesis of subnanometric HEOs (Fig. 7(a)) [49].

Inspired by the CNCA strategy, POMs can be introduced to capture the HEO nuclei by direct bonding during the initial formation and then coassemble into 1D SNMs. Owing to the high exposed atom ratio, the resulting HEO-POM 1D SNMs contain abundant active sites, whereas POMs can act as electron buffer sponges to promote electron delocalization across the whole SNMs. As shown in Fig. 7(a) [49], the formation probability is dominated by the relative contributions of S_{vib}, S_{tra}, and S_{rot}. When ΔS_{tra} decreases, extra ΔS_{vib} compensates for the high ΔS_{sur}; therefore, more atoms are exposed on the surface, thus facilitating the formation of SNWs. Meanwhile, gain in S_{tra} drives the directional ordering of constituent units, thereby leading to the emergence of an SNB morphology. Moreover, the change in S_{rot} can affect the formation of subnanospirals and subnanocoils.

Controlled incorporation of multiple immiscible metal oxides ranging from CeO_x to $CoZnCuNiFeZrCeO_x$ into SNWs was achieved by adding PMA clusters under medium-temperature conditions (Fig. 7(b)) [50]. Energy-dispersive X-ray spectroscopy (EDS) mapping corroborated the homogeneous codistribution of all elemental components in the HEO-PMA SNWs, demonstrating the successful formation of a uniform, multielement architecture at the subnanometer scale (Fig. 7(c)). When employed as anodes for sodium-ion batteries, these HEO-PMA SNWs delivered outstanding electrochemical performance. Notably, the $CoZnCuNiFeZrCeO_x$-PMA SNWs exhibited a higher specific capacity and a lower initial capacity loss (Fig. 7(d)). The rich defects and sites formed by the high-entropy composition provided a greater number of reversible storage sites, enhancing sodium-ion

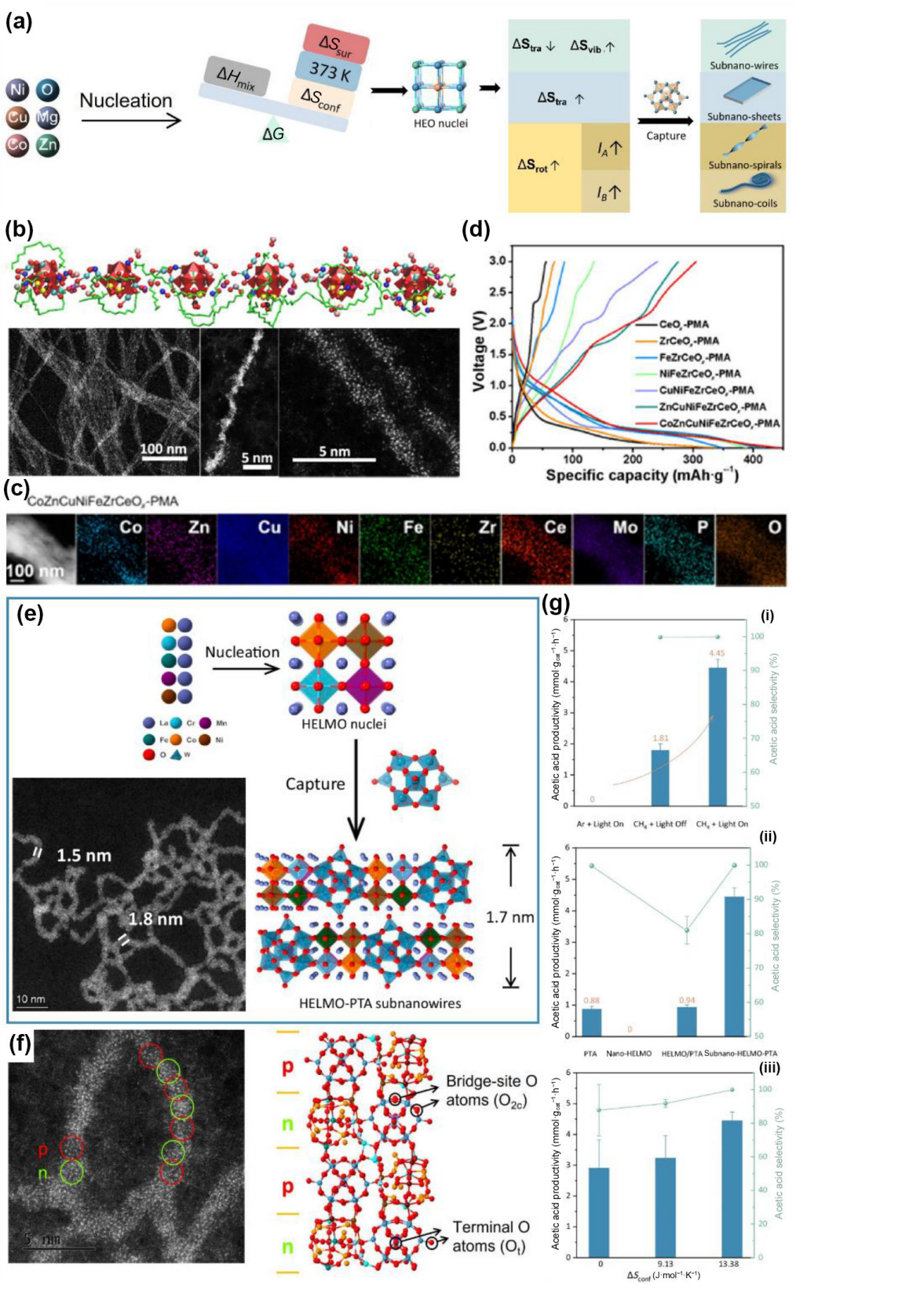

Figure 7 HEO-POM 1D SNMs. (a) Scheme of the synthesis of sub-nanometric HEO. Reproduced or adapted with permission from Ref. [49], © Nie, S. Y. 2026. (b) Molecular model and TEM images of HEO-POM SNWs. (c) EDS elemental mappings of $CoZnCuNiFeZrCeO_x$-PMA SNWs. (d) Galvanostatic initial discharging/charging curves for all kinds of HEO-POM SNWs at 0.1 C. Reproduced or adapted with permission from Ref. [50], © American Chemical Society 2022. (e) Schematic illustration of the process of subnano-HELMO-PTA SNWs. (f) Atomic-resolution high-angle annular dark-field (HAADF)-STEM image and scheme of the $(–p–n–p–n–)_n$ type heteroconstruction of subnano-HELMO-PTA. (g) PEC coupling of CH_4 performance. Reproduced or adapted with permission from Ref. [51], © Nie, S. Y., et al. 2024.

transport rate and charge transfer kinetics, thereby improving specific capacity and rate performance. Moreover, benefiting from the entropy-stability effect, the high-entropy composition creates an inherently stable framework that preserves the active material for subsequent cycling.

In SNWs, electrons can be shared between adjacent structural units, leading to electron delocalization that renders their electronic structures highly tailorable, which is beneficial for the catalytic activity. Recently, using a core–shell-mediated low-temperature approach, subnano high-entropy $LaMnO_3$-type perovskite-phosphotungstic acid (subnano-HELMO-PTA) SNWs possessing a well-defined long-range $(–p–n–p–n–)_n$ heterostructure were designed and fabricated (Figs. 7(e) and 7(f)) [51]. These subnano-HELMO-PTA SNWs demonstrated excellent catalytic performance in the photoelectrochemical (PEC) coupling of methane, achieving a high acetate yield of up to 4.45 $mmol·g^{-1}·h^{-1}$ with > 99% selectivity (Fig. 7(g)). The high-entropy design simultaneously enhances catalytic activity and stability through lattice distortion and an increase in configurational entropy. This boosted activity was further reinforced by the inherently sluggish diffusion kinetics, which effectively suppressed structural rearrangement and ensured stability under catalytic conditions. This unique alternating configuration establishes a built-in electronic field that promotes interfacial charge transfer, while the high-entropy character induces lattice distortion and configurational complexity, which synergistically enhance structural integrity and functional versatility, particularly in catalytic and energy conversion applications.

Overall, the components and structures of POM-based 1D SNMs can be precisely controlled to achieve tailored properties, making them suitable models for investigating structure–property relationships. The high-dimensional similarity to polymer chains endows POM-based 1D SNMs with superior processability and mechanical performance, rendering them promising for SNM-based fibers, films, and organogels. In addition, POM-based 1D SNMs exhibit large-scale electron delocalization, enabling fast charge transfer and outstanding catalytic activity.

3 Conclusion and outlook

This review summarizes recent progress on the precise synthesis and applications of POM-based 1D SNMs (Table S1 in the Electronic Supplementary Material (ESM)). POM clusters filled with coordinated oxygen sites are ideal building blocks for the fabrication of 1D SNMs, whose components and electronic structures can be precisely controlled to achieve tailored properties. Using POM clusters as building blocks, diverse multiple-component 1D SNMs have been synthesized, including POM 1D SNMs, M-POM 1D SNMs, M^{n+}-POM 1D SNMs, M_xO_y-POM 1D SNMs, M_xS_y-POM 1D SNMs, and HEO-POM 1D SNMs. These materials can be synthesized via two main approaches: the good–poor solvent method and the CNCA strategy (Scheme S1 in the ESM). These POM-based 1D SNMs typically exhibit ultrahigh specific surface area with a single-unit-cell width or thickness, in addition to excellent flexibility owing to their similar size and topology to polymer chains. By virtue of their distinctive electronic properties, POMs drive electron transfer across whole nuclei-cluster building blocks, leading to large-scale electron delocalization in 1D SNMs, which provides a fundamental platform for unique properties in catalysis, charge transfer, and photothermal/electrochemical energy conversion fields. In addition, POM-based 1D SNMs exhibit superior processability, enabling the formation of elastic gels and tough films that enhance their functional versatility.

Although POM-based 1D SNMs offer tunable structures and properties to meet diverse applications, considerable challenges remain. First, an in-depth investigation of the structure–property relationship is fundamental to the rational design and preparation of 1D SNMs. Previously, research on 1D SNMs has disproportionately focused on morphological features, often at the expense of understanding the electronic structure and its functional implications, thereby neglecting opportunities to elucidate key structure–property relationships essential for practical applications. Second, currently, POM clusters used as building blocks are mainly Mo/W-based POMs, which only work under neutral or acidic conditions. Therefore, the development of Nb/Ta-based POMs suitable for basic conditions would be desirable for the growth and assembly of 1D SNMs. Future research efforts should focus on preparing 1D SNMs with functional versatility. The synergistic effect of components in 1D SNMs facilitates versatility. Although diverse HEO components have demonstrated remarkable functional properties, the full potential of these complex systems remains untapped in the absence of standardized analytical frameworks, having to resort to computational modeling and machine learning to predict structure–property relationships. In fact, the investigation of other multicomponent POM-based 1D SNMs remains highly challenging. In addition, although the polymer-like properties of SNWs are attractive for processing, practical methods for their macroscopic assembly are scarce. Finally, owing to their ultrahigh surface energy, 1D SNMs exhibit partial instability under electron beam irradiation and thus require single and indirect characterization techniques to clearly identify their structure. There is also a need to explore 1D SNMs with robust structures that resist electron beam irradiation. The intrinsic chirality of POMs and SNBs endows them with excellent polarization properties in optical devices. However, precise control over the chirality of POM-based 1D SNMs is difficult. At present, much effort is devoted to the programmable, predictable chirality of POM-based 1D SNMs and to exploring their application in chiral catalysis.

In summary, POMs have emerged as essential building blocks for the rational design of 1D SNMs, greatly influencing their synthesis, properties, and performance. In 1D SNMs, the unique electronic properties of POMs induce large-scale electron delocalization throughout the SNMs, and their dimensional similarity to polymer chains confers superior flexibility, processability, and self-assembly behavior. Moreover, the synergistic effects of POM clusters and metal species have enabled the development of HEO-POM 1D SNMs with enhanced structural stability and tailored properties. These features collectively contribute to their remarkable performance, positioning POM-based 1D SNMs as advanced materials for gelling, adhesion, catalysis, photoelectric response, and photothermal conversion applications.

Electronic Supplementary Material: Supplementary material is available in the online version of this article at https://doi.org/10.26599/POM.2026.9140117.

Data availability

Not applicable.

Acknowledgements

This work was supported by the National Natural Science Foundation of China (Nos. 22422501 and 22375018).

Declaration of competing interest

The authors declare no competing financial interest.

Author contribution statement

Y. F. Q. was involved in writing manuscript. R. Z. M. assisted with the collection of materials. S. M. Z. proposed and designed the project, revised and determined the manuscript. All the authors have approved the final manuscript.

Use of AI statement

None.

References

[1] Liu, Q. D.; Wang, X. Y.; Wang, X. Sub‐1 nm materials chemistry: Challenges and prospects. *J. Am. Chem. Soc.* **2024**, *146*, 26587–26602.

[2] Ni, B.; Shi, Y. A.; Wang, X. The sub-nanometer scale as a new focus in nanoscience. *Adv. Mater.* **2018**, *30*, 1802031.

[3] Ni, B.; Wang, X. Chemistry and properties at a sub-nanometer scale. *Chem. Sci.* **2016**, *7*, 3978–3991.

[4] Hu, S.; Wang, X. Ultrathin nanostructures: Smaller size with new phenomena. *Chem. Soc. Rev.* **2013**, *42*, 5577–5594.

[5] Wang, H. L.; Li, J.; Zhu, H. W. Ultimate structures in catalysis: Single atoms, subnano-clusters, and electrons. *Sci. China Mater.* **2023**, *66*, 4521–4541.

[6] Nie, S. Y.; Wang, X. Electron delocalization and transfer across polyoxometalates-based subnanomaterials in catalytic reactions. *Small Methods* **2024**, *8*, 2301359.

[7] Li, Z.; Li, H. Y.; Lin, Y.; Shi, W. X.; Wang, X. Cluster-cation pairs mediated assembly of subnanometer polyoxometalates superstructures. *J. Am. Chem. Soc.* **2024**, *146*, 28874–28884.

[8] Lu, Q. C.; Huang, B. L.; Zhang, Q. H.; Chen, S. M.; Gu, L.; Song, L.; Yang, Y.; Wang, X. Single-crystal inorganic helical architectures induced by asymmetrical defects in sub-nanometric wires. *J. Am. Chem. Soc.* **2021**, *143*, 9858–9865.

[9] He, J.; Liu, H. L.; Xu, B.; Wang, X. Highly flexible sub-1 nm tungsten oxide nanobelts as efficient desulfurization catalysts. *Small* **2015**, *11*, 1144–1149.

[10] Yang, Y.; Yang, Y.; Chen, S. M.; Lu, Q. C.; Song, L.; Wei, Y.; Wang, X. Atomic-level molybdenum oxide nanorings with full-spectrum absorption and photoresponsive properties. *Nat. Commun.* **2017**, *8*, 1559.

[11] Zhang, S. M.; Wang, X. Sub-1 nm: A critical feature size in materials science. *Acc. Mater. Res.* **2022**, *3*, 1285–1298.

[12] Hu, S.; Liu, H. L.; Wang, P. P.; Wang, X. Inorganic nanostructures with sizes down to 1 nm: A macromolecule analogue. *J. Am. Chem. Soc.* **2013**, *135*, 11115–11124.

[13] Zhang, S. M.; Shi, W. X.; Yu, B.; Wang, X. Versatile inorganic subnanometer nanowire adhesive. *J. Am. Chem. Soc.* **2022**, *144*, 16389–16394.

[14] Xu, X. X.; Zhuang, J.; Wang, X. SnO_2 quantum dots and quantum wires: Controllable synthesis, self-assembled 2D architectures, and gas-sensing properties. *J. Am. Chem. Soc.* **2008**, *130*, 12527–12535.

[15] Wang, P. P.; Yang, Y.; Zhuang, J.; Wang, X. Self-adjustable crystalline inorganic nanocoils. *J. Am. Chem. Soc.* **2013**, *135*, 6834–6837.

[16] Zhang, S. M.; Shi, Y. A.; He, T.; Ni, B.; Li, C. Z.; Wang, X. Ultrathin tungsten bronze nanowires with efficient photo-to-thermal conversion behavior. *Chem. Mater.* **2018**, *30*, 8727–8731.

[17] Ni, B.; Zhang, Q. H.; Ouyang, C.; Zhang, S. M.; Yu, B.; Zhuang, J.; Gu, L.; Wang, X. The synthesis of sub-nano-thick Pd nanobelt-based materials for enhanced hydrogen evolution reaction activity. *CCS Chem.* **2020**, *2*, 642–654.

[18] Liu, J. L.; Shi, W. X.; Ni, B.; Yang, Y.; Li, S. Z.; Zhuang, J.; Wang, X. Incorporation of clusters within inorganic materials through their addition during nucleation steps. *Nat. Chem.* **2019**, *11*, 839–845.

[19] Sinyagin, A. Y.; Belov, A.; Tang, Z.; Kotov, N. A. Monte Carlo computer simulation of chain formation from nanoparticles. *J. Phys. Chem. B* **2006**, *110*, 7500–7507.

[20] Liu, J. L.; Liu, N.; Wang, H. W.; Shi, W. X.; Zhuang, J.; Wang, X. Hybrid MoO_3-polyoxometallate sub-1 nm nanobelt superstructures. *J. Am. Chem. Soc.* **2020**, *142*, 17557–17563.

[21] Liu, J. L.; Wang, S. B.; Liu, N.; Yang, D. R.; Wang, H. W.; Hu, H. S.; Zhuang, J.; Wang, X. Au-polyoxometalates A-B-A-B type copolymer-analogue sub-1 nm nanowires. *Small* **2021**, *17*, e2006260.

[22] Liu, Q. D.; He, S. Q.; Yu, B.; Cheng, X. J.; Shi, W. X.; Wang, X. Visible light induced Ag-polyoxometalate coassembly into single-cluster nanowires. *Adv. Mater.* **2022**, *34*, e2206178.

[23] Zhang, S. M.; Lu, Q. C.; Yu, B.; Cheng, X. J.; Zhuang, J.; Wang, X. Polyoxometalates facilitating synthesis of subnanometer nanowires. *Adv. Funct. Mater.* **2021**, *31*, 2100703.

[24] Cai, Q. M.; Gao, R. L.; Wang, Y. F.; Xing, J. S.; Zhang, Q. Y.; Zhu, M. Z.; Qin, X. Y.; Liao, M. H.; Huang, Y. C. Ruthenium containing polyoxometalates: From synthesis, structures, properties to functional applications. *Polyoxometalates* **2025**, *4*, 9140083.

[25] Liu, Q. D.; Yu, H. D.; Zhang, Q. H.; Wang, D.; Wang, X. Temperature-responsive self-assembly of single polyoxometalates clusters driven by hydrogen bonds. *Adv. Funct. Mater.* **2021**, *31*, 2103561.

[26] Kong, H.; Ma, P. T.; Wang, J. P.; Niu, J. Y. Overview of organophosphonate covalently modified polyoxometalates: From synthesis and structural diversity to applications. *Polyoxometalates* **2025**, *4*, 9140103.

[27] Anyushin, A. V.; Kondinski, A.; Parac-Vogt, T. N. Hybrid polyoxometalates as post-functionalization platforms: From fundamentals to emerging applications. *Chem. Soc. Rev.* **2020**, *49*, 382–432.

[28] Liu, Q. D.; He, P. L.; Yu, H. D.; Gu, L.; Ni, B.; Wang, D.; Wang, X. Single molecule-mediated assembly of polyoxometalate single-cluster rings and their three-dimensional superstructures. *Sci. Adv.* **2019**, *5*, eaax1081.

[29] Liu, Q. D.; Zhang, Q. H.; Shi, W. X.; Hu, H. S.; Zhuang, J.; Wang, X. Self-assembly of polyoxometalate clusters into two-dimensional clusterphene structures featuring hexagonal pores. *Nat. Chem.* **2022**, *14*, 433–440.

[30] Ma, R. Z.; Shi, W. X.; Qin, Y. F.; Qi, S. G.; Zhang, S. M. Sustained metal ion release-controlled synthesis of polyoxometalate subnanowires. *Small Methods* **2025**, *9*, e00825.

[31] Liu, Q. D.; Wang, X. Sub-nanometric materials: Electron transfer, delocalization, and beyond. *Chem Catal.* **2022**, *2*, 1257–1266.

[32] Liu, H. L.; Li, H. Y.; He, P. L.; Wang, X. Sub-1 nm nickel molybdate nanowires as building blocks of flexible paper and electrochemical catalyst for water oxidation. *Small* **2016**, *12*, 1006–1012.

[33] Ge, H. Y.; Zhang, F. H.; Hao, Z. M.; Liu, J. L.; Zhang, Y.; Wang, X. A universal strategy to increase the mechanical performance of polymer-inorganic composites by sub-1 nm hetero-nanowires. *Adv. Funct. Mater.* **2025**, *35*, 2422768.

[34] Cheng, X. J.; Nie, S. Y.; Huang, Y.; Liu, Q. D.; Wu, L.; Wang, X. Electron-delocalization across high surface entropy Sub-1 nm nanobelts toward enhanced electrocatalytic urea oxidation. *Small* **2024**, *20*, e2404595.

[35] Liu, Q. D.; Sheng, Z.; Shi, W. X.; Cheng, X. J.; Xu, X. X.; Wang, X.

Tuning the chirality evolution in achiral subnanometer systems by judicious control of molecule interactions. *J. Am. Chem. Soc.* **2024**, *146*, 12819–12827.
[36] Liu, Q. D.; Wang, X. Precise assembly of polyoxometalates at single-cluster levels. *Angew. Chem., Int. Ed.* **2023**, *62*, e202217764.
[37] Yang, W. Z.; Liu, Y. J.; Wang, M. Y.; Wang, X. Y.; Liu, Q. D.; Lan, L. J.; Yin, P. C.; Zhan, C. H.; Jiang, Z. G.; Wang, X. Giant five-shell polyoxometalate cages and the single-cluster-based nanowire superstructures. *J. Am. Chem. Soc.* **2025**, *147*, 25990–25997.
[38] Qian, D. Q.; Lin, Y. D.; Xiao, H. P.; Wu, B.; Li, X. X.; Zheng, S. T. Advances in coinage-metal-substituted polyoxometalates: A review. *Polyoxometalates* **2024**, *3*, 9140040.
[39] Car, P. E.; Spingler, B.; Weyeneth, S.; Patscheider, J.; Patzke, G. R. All-inorganic 1D chain-based architecture of a novel dimanganese-substituted Keggin polyoxotungstate. *Polyhedron* **2013**, *52*, 151.
[40] Li, Z.; Huang, Y. W.; Li, H. Y.; Zhang, F. H.; Ren, Y. Z.; Shi, W. X.; Liu, Q. D.; Wang, X. Single-walled cluster nanotubes for single-atom catalysts with precise structures. *J. Am. Chem. Soc.* **2024**, *146*, 450–459.
[41] Guan, Y.; Xiao, H. P.; Li, X. X.; Zheng, S. T. Recent advances on the synthesis, structure, and properties of polyoxotantalates. *Polyoxometalates* **2023**, *2*, 9140023.
[42] Zhang, S. M.; Shi, W. X.; Wang, X. Locking volatile organic molecules by subnanometer inorganic nanowire-based organogels. *Science* **2022**, *377*, 100–104.
[43] Zhang, F. H.; Li, Z.; Wang, X. Mechanically tunable organogels from highly charged polyoxometalate clusters loaded with fluorescent dyes. *Nat. Commun.* **2023**, *14*, 8327.
[44] Izzet, G.; Abécassis, B.; Brouri, D.; Piot, M.; Matt, B.; Serapian, S. A.; Bo, C.; Proust, A. Hierarchical self-assembly of polyoxometalate-based hybrids driven by metal coordination and electrostatic interactions: From discrete supramolecular species to dense monodisperse nanoparticles. *J. Am. Chem. Soc.* **2016**, *138*, 5093–5099.
[45] Zhang, S. M.; Shi, H. D.; Tang, J. W.; Shi, W. X.; Wu, Z. S.; Wang, X. Super-aligned films of sub-1 nm Bi_2O_3-polyoxometalate nanowires as interlayers in lithium-sulfur batteries. *Sci. China Mater.* **2021**, *64*, 2949–2957.
[46] Zhang, S. M.; Liu, N.; Wang, H. W.; Lu, Q. C.; Shi, W. X.; Wang, X. Sub-nanometer nanobelts based on titanium dioxide/zirconium dioxide-polyoxometalate heterostructures. *Adv. Mater.* **2021**, *33*, 2100576.
[47] Fu, H.; Xu, Y. Z.; Qiu, D.; Ma, T. F.; Yue, G. L.; Zeng, Z. C.; Song, L. P.; Wang, S. Y.; Zhang, S.; Du, Y. P. et al. A library of rare earth oxide ultrathin nanowires with polymer-like behaviors. *Angew. Chem., Int. Ed.* **2022**, *61*, e202212251.
[48] Yang, D. R.; Zou, S. W.; Yang, H. Z.; Wang, X. Single-unit-cell catalysis of CO_2 electroreduction over sub-1 nm Cu_9S_5 nanowires. *Adv. Energy Mater.* **2021**, *11*, 2100272.
[49] Nie, S. Y.; Liu, Q. D.; Wu, L.; Wang, X. Surface entropy-engineering: Towards general synthesis of high entropy subnano-oxides. *Nano Res.* **2026**, *19*, 94908030.
[50] Liu, J. L.; Li, Y. Q.; Chen, Z.; Liu, N.; Zheng, L. R.; Shi, W. X.; Wang, X. Polyoxometalate cluster-incorporated high entropy oxide sub-1 nm nanowires. *J. Am. Chem. Soc.* **2022**, *144*, 23191–23197.
[51] Nie, S. Y.; Wu, L.; Zhang, Q. H.; Huang, Y. W.; Liu, Q. D.; Wang, X. High-entropy-perovskite subnanowires for photoelectrocatalytic coupling of methane to acetic acid. *Nat. Commun.* **2024**, *15*, 6669.

Yifan Qin is pursuing her Ph.D. degree in chemical engineering and technology at Beijing Institute of Technology (BIT). Her current research focuses on the synthesis and assembly behavior of subnanowires.

Rongzhu Ma is currently pursuing her Ph.D. degree in chemistry at School of Chemistry and Chemical Engineering, Beijing Institute of Technology (BIT), Beijing, China. Her research interests include the synthesis and assembly methods of subnanowires.

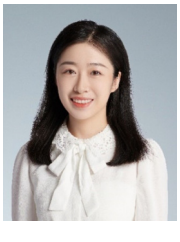

Simin Zhang received her Ph.D. degree in chemistry from Tsinghua University in 2020. She is currently a professor with the School of Chemistry and Chemical Engineering, Beijing Institute of Technology (BIT), Beijing, China. Her current research focuses on the synthesis and application of sub-1 nm nanowires/nanobelts.